Electronic Supplementary Material (ESI) for Journal of Materials Chemistry A.
This journal is © The Royal Society of Chemistry 2020

Metal-organic framework-derived carbon as the positive electrode for high-performance vanadium redox flow batteries

*Yang Li,[a] Lianbo Ma,[a] Zhibin Yi,[a] Yunhe Zhao,[a] Jiatao Mao,[b] Shida Yang,[b] Wenqing Ruan,[b] Diwen Xiao,[a] Nauman Mubarak,[a] Junxiong Wu,[a] Tian-Shou Zhao,[a] Qing Chen,[*ab] and Jang-Kyo Kim[*a]*

[a] Department of Mechanical and Aerospace Engineering, The Hong Kong University of Science and Technology, Clear Water Bay, Hong Kong, China

[b] Department of Chemistry, The Hong Kong University of Science and Technology, Clear Water Bay, Hong Kong, China

* Corresponding author information:
E-mail: chenqing@ust.hk (Qing Chen)
Email: mejkkim@ust.hk (Jang-Kyo Kim)

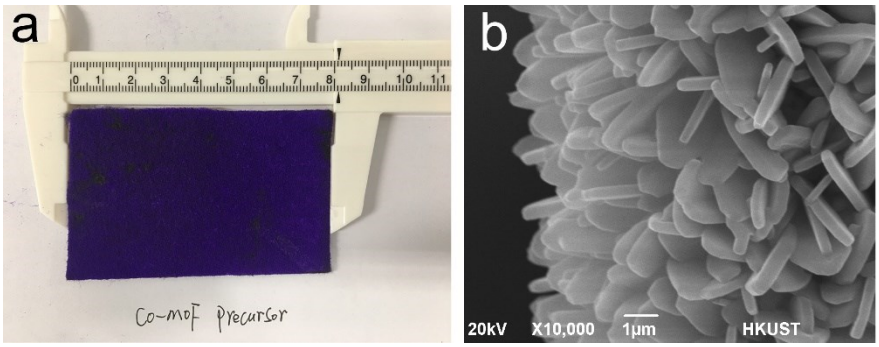

Fig. S1. (a) Optical image of MOF film with a size of 6 cm×8 cm and (b) SEM images of MOF precursor;

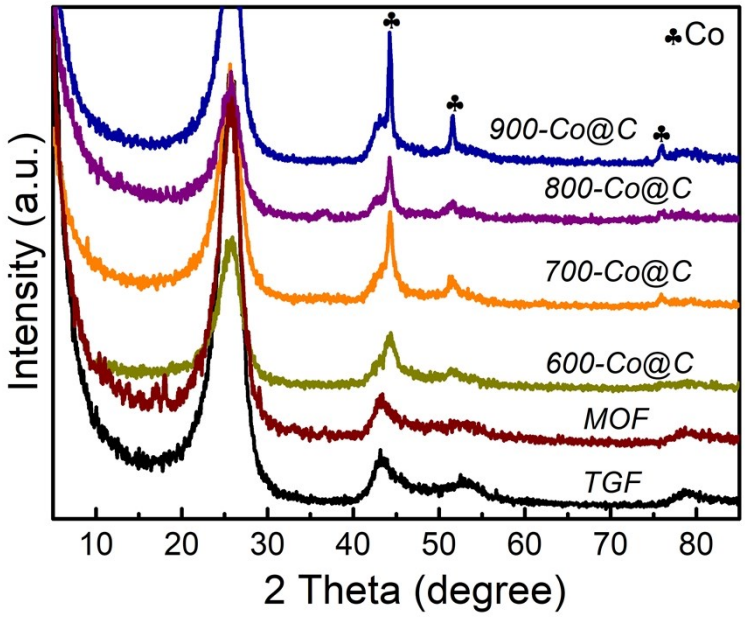

Fig. S2. XRD patterns of MOF precursor and Co@C obtained at different carbonization temperatures.

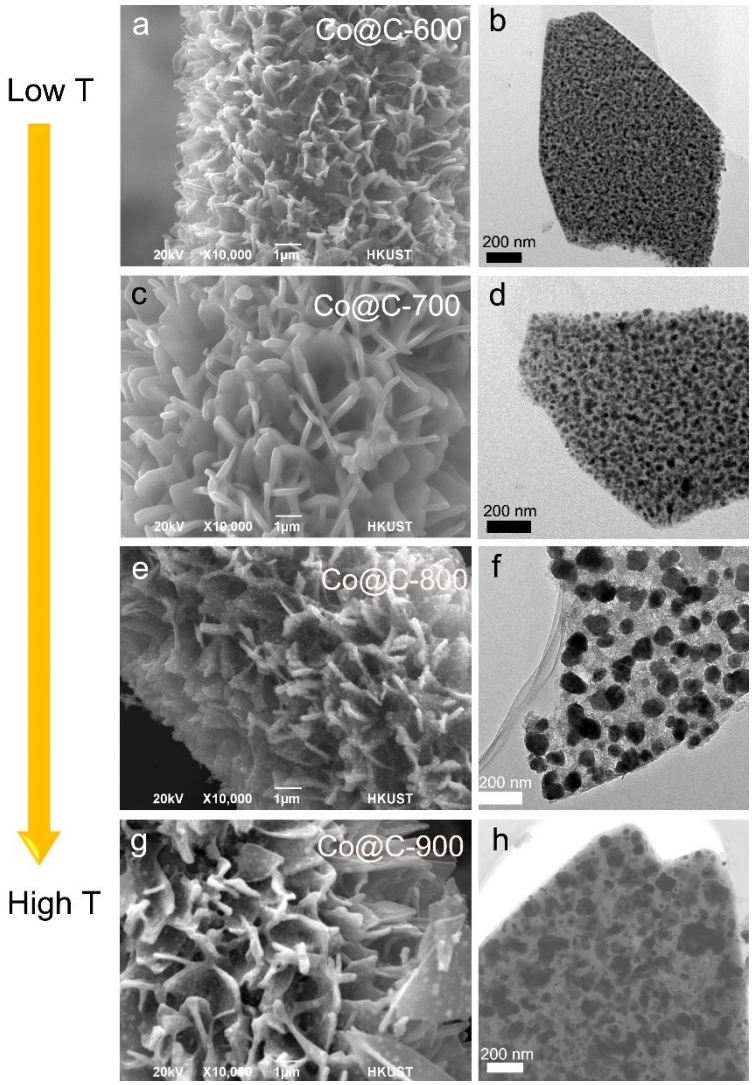

Fig. S3. SEM and TEM images of (a-b) Co@C-600; (c-d) Co@C-700; (e-f) Co@C-800; (g-h) Co@C-900.

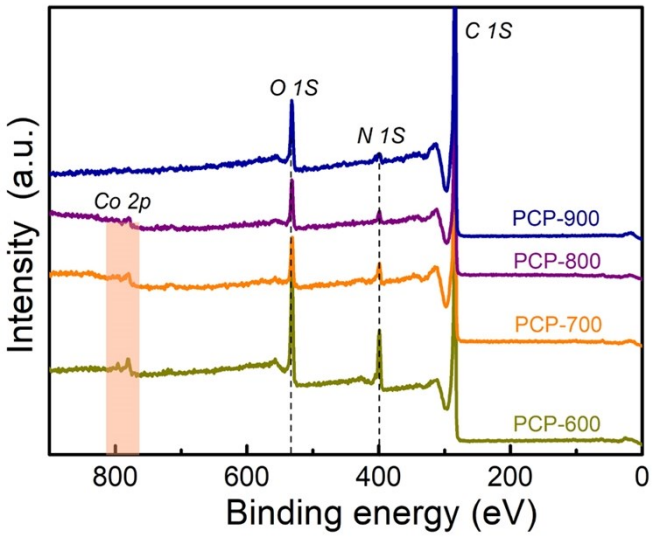

Fig. S4. Survey XPS spectra of PCPs prepared at different carbonization temperatures.

Table S1. Elemental compositions (at %) of PCPs.

Samples	***C***	***O***	***N***	***Co***
PCP-600	77.13	11.58	10.74	0.55
PCP-700	91.06	4.85	3.58	0.51
PCP-800	91.66	5.44	2.52	0.38
PCP-900	92.75	5.62	1.38	0.25

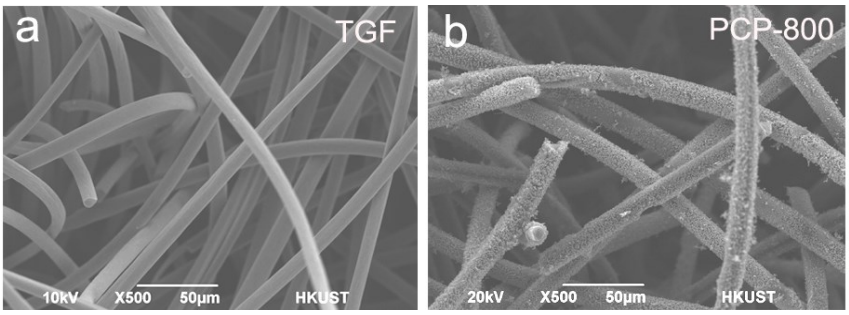

Fig. S5. SEM images of (a) TGF and (b) PCP-800.

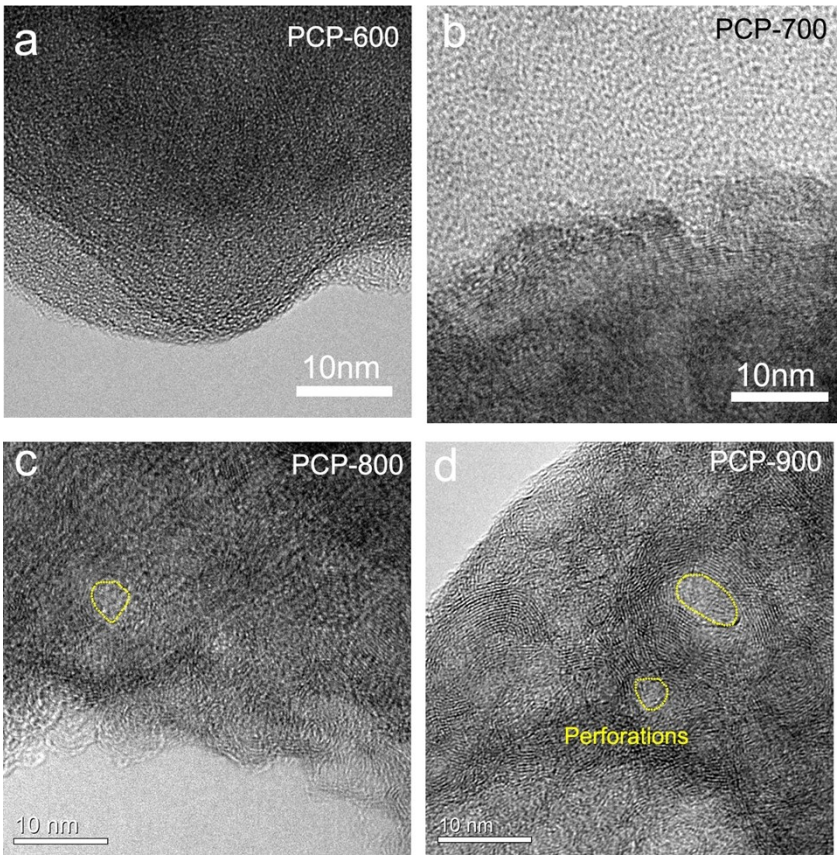

Fig. S6. High-resolution TEM images of PCPs obtained at different carbonization temperatures.

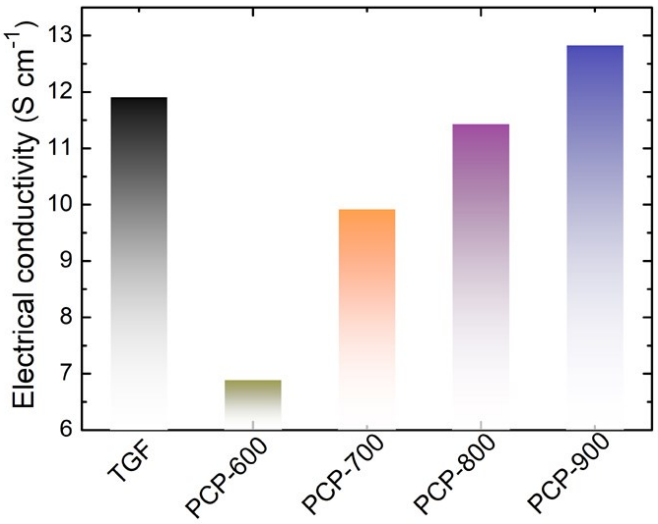

Fig. S7. Electrical conductivity of TGF and PCPs.

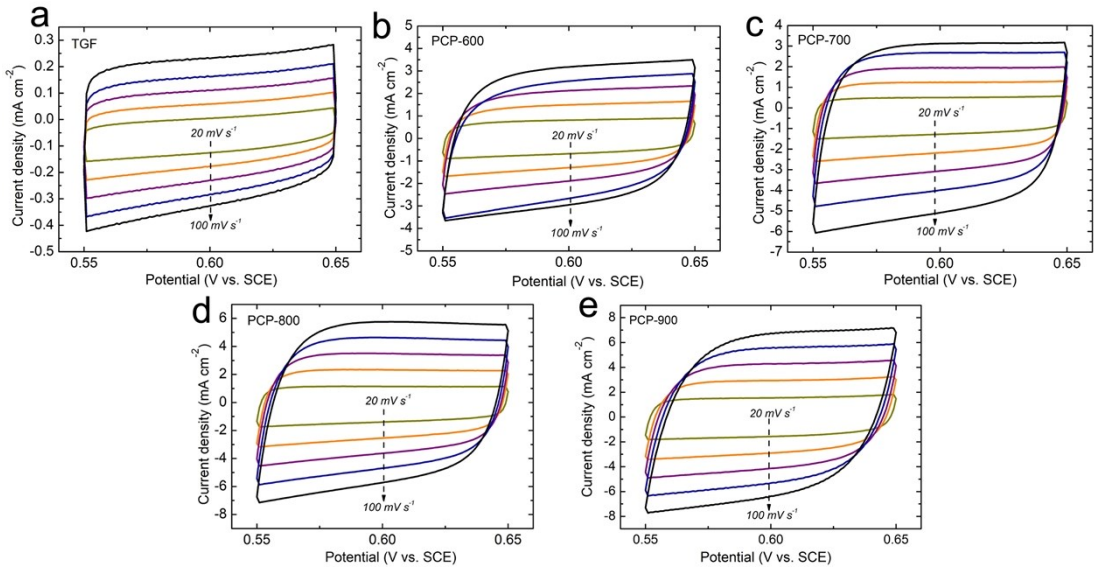

Fig. S8. CV curves of the TGF and PCP electrodes recorded at different scan rates in a non-Faradic region.

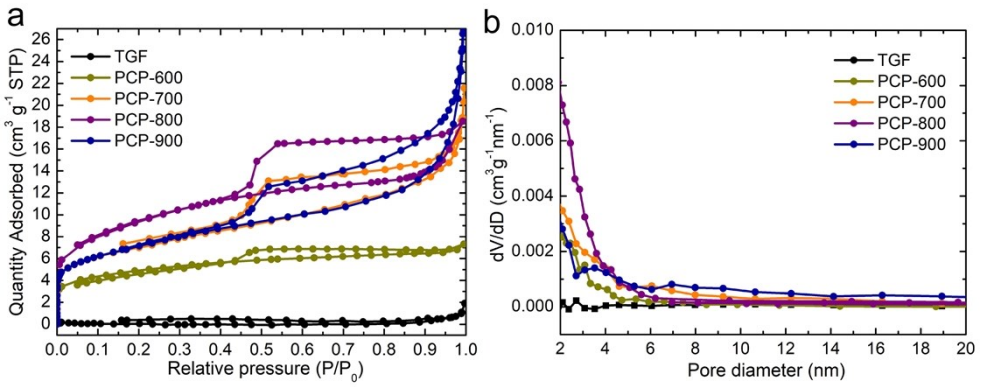

Fig. S9. (a) Nitrogen adsorption/desorption isotherms; (b) BJH pore distribution curves.

Table S2. BET surface area and pore volume of PCPs.

Materials	***BET surface area (m^2 g^{-1})***	***Pore volume (cm^3 g^{-1})***
TGF	0.46	0.00170
PCP-600	16.37	0.0101
PCP-700	25.38	0.0238
PCP-800	32.73	0.0284
PCP-900	25.68	0.0372

The BET results are basically consistent with the ECSA's results with the pore volume and surfacec area positively changing with increasing carbonization temperature. One special case is the PCP-900 electrode. Becasue it has a relatively loose structure with a large pore volume, it could easily collapse during the BET test but remain stable in the nondestructive CV test, leading to the disparity between the BET and ECSA.

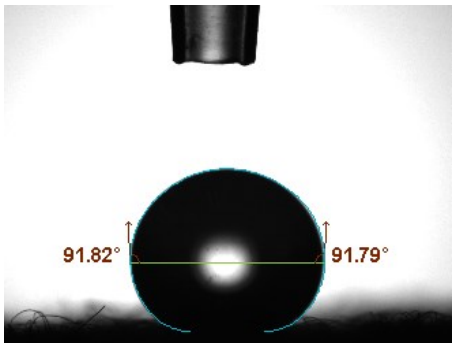

Fig. S10. Electrolyte accessibility test of neat graphite felt.

Table S3. Key structural and functional parameters of PCPs prepared at different carbonization temperatures.

Materials	*Structural features*				*Functional features*			
	Electrical conductivities ($S\ cm^{-1}$)	*Surface Area ($m^2\ g^{-1}$)*	*Pore Volume ($cm^3\ g^{-1}$)*	*ECSA ($mF\ cm^{-2}$)*	*I_D/I_G*	*Oxygen (at%)*	*Nitrogen (at%)*	*Vacancy/sp^2*
PCP-600	6.89	16.37	0.0101	29.3	1.89	11.58	10.74	0.37
PCP-700	9.92	25.38	0.0238	40.3	1.72	4.85	3.58	0.33
PCP-800	**11.43**	**32.73**	**0.0284**	**55.8**	**1.60**	**5.44**	**2.52**	**0.31**
PCP-900	12.83	25.68	0.0372	62.6	1.34	5.62	1.38	0.18

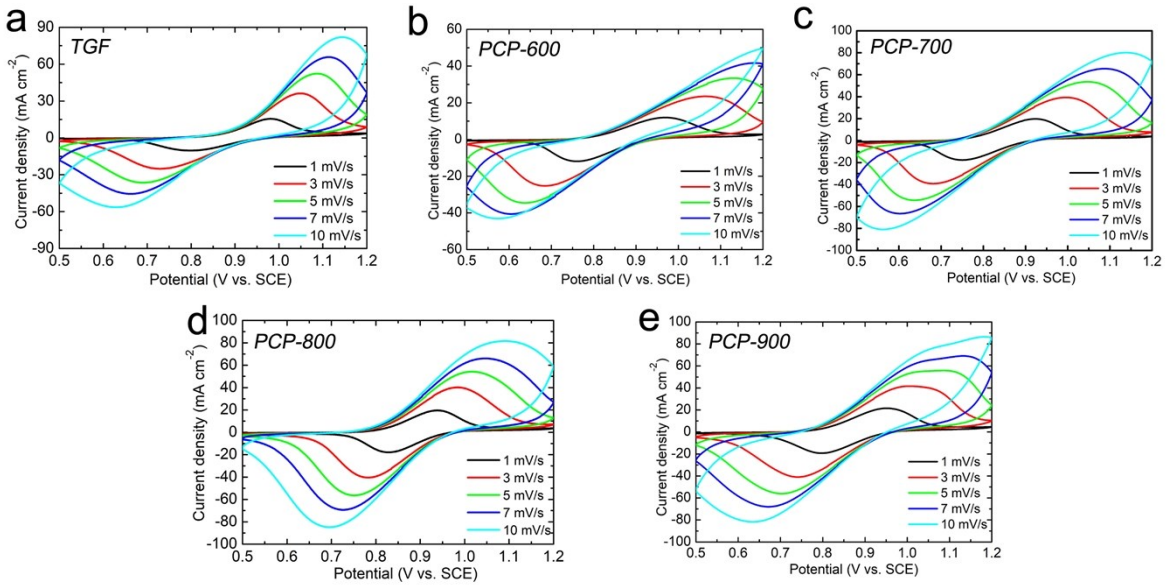

Fig. S11. CV curves of TGF and PCPs recorded at different scan rates.

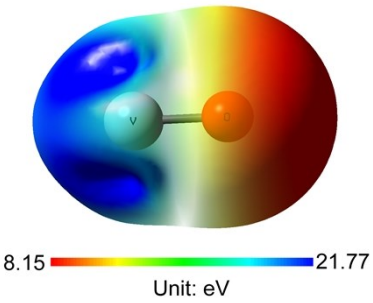

Fig. S12. Electrostatic potential map of VO^{2+}.

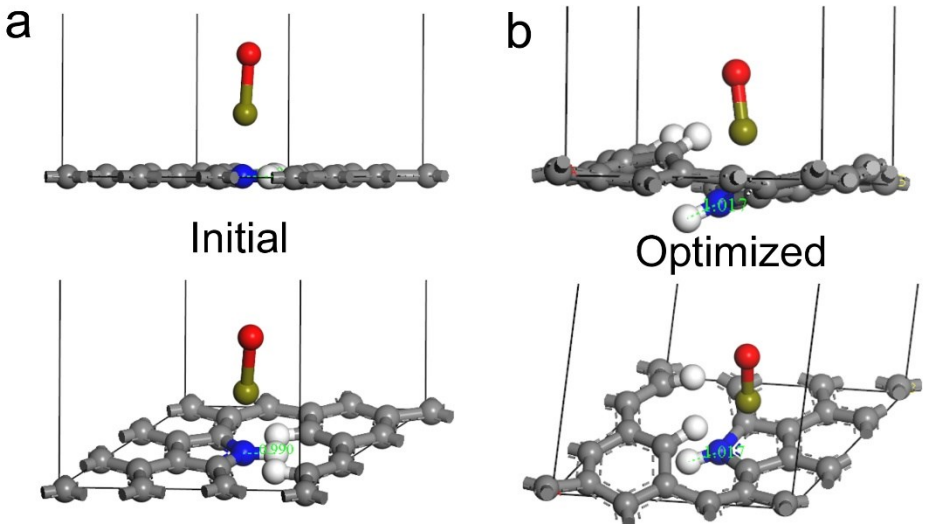

Fig. S13. (a) Initial structure of vanadium-oxygen moiety adsorbed on pyrrolic-N and (b) optimized structure.

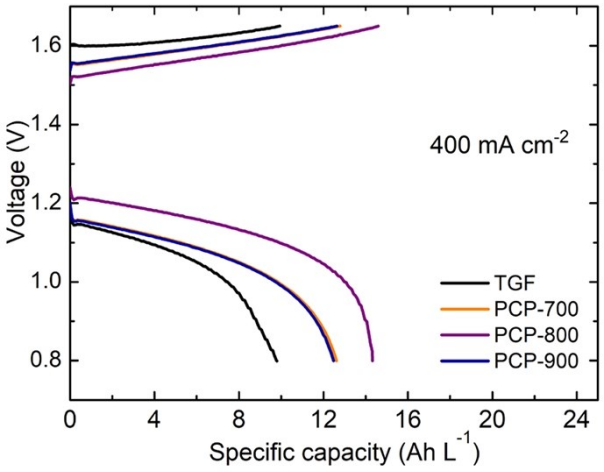

Fig. S14. Charge and discharge curves of the TGF and PCP electrodes measured at 400 mA cm^{-2}.

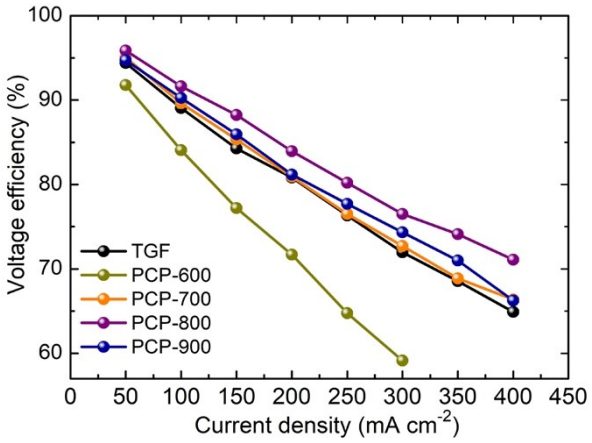

Fig. S15. Voltage efficiencies of the TGF and PCP electrodes.

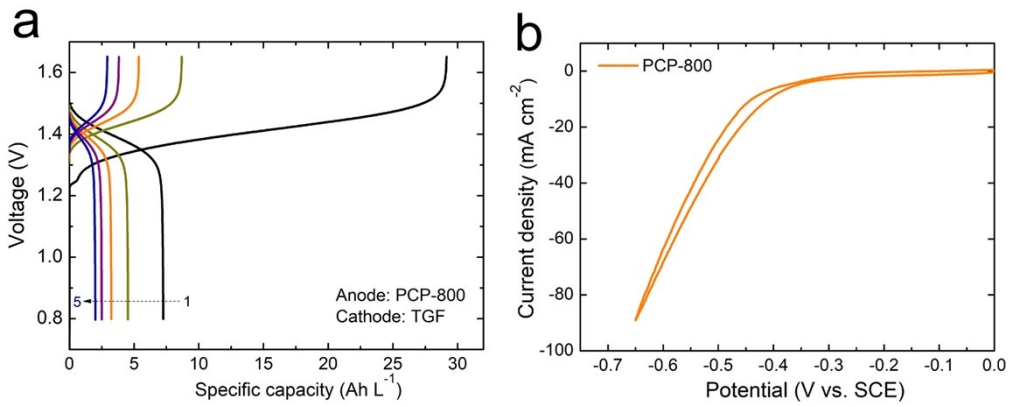

Fig. S16. (a) Charge-discharge curves of VRFBs with PCP-800 as the negative electrode and TGF as the positive electrode at a current density of 50 mA cm^{-2}. (b) CV curves of PCP-800 in three-electrodes system.

As shown in Figure S16a, the flow batteries assembled with the PCP-800 as the negative electrode and thermal-treated graphite felt (TGF) as the positive electrode presented the poor capacity retention within 5 cycles. Notably, the initial charging capacity (29.1 mAh L^{-1}) was beyond the theoretical one (26.8 mAh L^{-1}), which is abnormal phenomenon in VRFBs. We attributed it to the side reaction, hydrogen evolution reaction (HER), inducing the charge imbalance and undesirable efficiency loss. Although a long-time acid-etching process was involved in this work, there were indeed some remaining Co embedded in the PCP electrode, which was proved by the XPS and TEM image (Figure S4 and Figure 3f). Co-containing carbon electrodes are known to function as electrocatalysts towards HER. CV further confirms that the MOF-derived electrode presented good catalytic activity towards HER, even suppressing the redox reaction of V^{3+}/V^{2+} (Figure S16b). In this case, our MOF-derived PCP electrode is more suitable for the positive electrode.

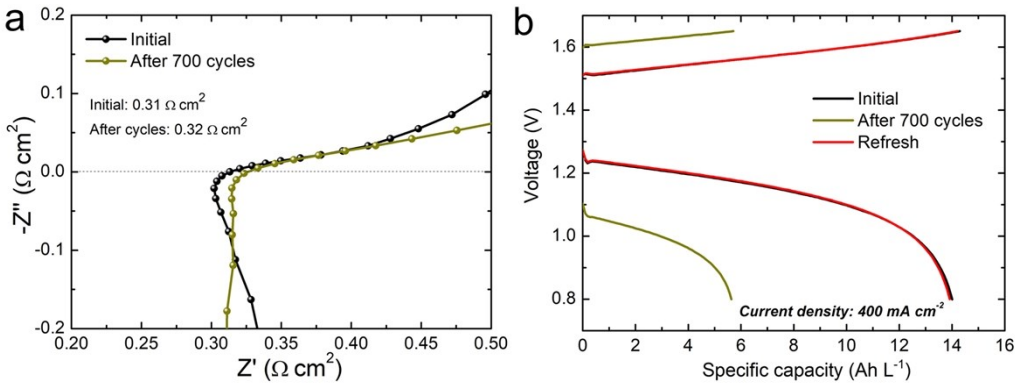

Fig. S17. (a) EIS spectra obtained before and after 700 cycles; and (b) Comparison of charge and discharge curves at different states: initial, 700-cycled and refreshed.

Table S4. Comparison of energy efficiencies between the current study and the state-of-the-art VRFBs.

Samples	Current density (mA cm^{-2})	Energy efficiency (%)	Reference
PCP-800	**200**	**82.0**	**This work**
	400	**69.7**	
HCN	250	70.4	1
GO-rGO/GF	50	87	2
rGO-2/GF	300	60	3
NCS	300	53	4
E-GnP	150	68	5
Nb-WO_3	80	78.10	6
Mxene/GF	200	81.3	7
H-PGF	300	57.3	8
Gradient-pore GF	400	68.72	9
N-CB	150	68.6	10
NGF-Co	150	74.2	11
GF@CN	200	64.1	12
Redox-Mediated Catalysis	360	51.87	13
B-GF	320	77.97	14
E-GF	100	86.41	15
Wood-derived carbon	40	75.44	16

References

1. W. Ling, Q. Deng, Q. Ma, H. R. Wang, C. J. Zhou, J. K. Xu, Y. X. Yin, X. W. Wu, X. X. Zeng and Y. G. Guo, *Adv. Sci.*, 2018, **5**, 1801281.
2. G. Hu, M. Jing, D.-W. Wang, Z. Sun, C. Xu, W. Ren, H.-M. Cheng, C. Yan, X. Fan and F. Li, *Energy Storage Mater.*, 2018, **13**, 66-71.
3. Q. Deng, P. Huang, W.-X. Zhou, Q. Ma, N. Zhou, H. Xie, W. Ling, C.-J. Zhou, Y.-X. Yin, X.-W. Wu, X.-Y. Lu and Y.-G. Guo, *Adv. Energy Mater.*, 2017, **7**, 1700461.
4. L. Wu, Y. Shen, L. Yu, J. Xi and X. Qiu, *Nano Energy*, 2016, **28**, 19-28.
5. M. Park, I.-Y. Jeon, J. Ryu, J.-B. Baek and J. Cho, *Adv. Energy Mater.*, 2015, **5**, 1401550.
6. D. M. Kabtamu, J.-Y. Chen, Y.-C. Chang and C.-H. Wang, *J. Mater. Chem. A*, 2016, **4**, 11472-11480.
7. L. Wei, C. Xiong, H. R. Jiang, X. Z. Fan and T. S. Zhao, *Energy Storage Mater.*, 2020, **25**, 885-892.
8. Y. Liu, Y. Shen, L. Yu, L. Liu, F. Liang, X. Qiu and J. Xi, *Nano Energy*, 2018, **43**, 55-62.
9. R. Wang, Y. Li and Y.-L. He, *J. Mater. Chem. A*, 2019, **7**, 10962-10970.
10. M. Park, J. Ryu, Y. Kim and J. Cho, *Energy Environ. Sci.*, 2014, **7**, 3727-3735.
11. S. Park and H. Kim, *J. Mater. Chem. A*, 2015, **3**, 12276-12283.
12. Q. Ma, X. X. Zeng, C. Zhou, Q. Deng, P. F. Wang, T. T. Zuo, X. D. Zhang, Y. X. Yin, X. Wu, L. Y. Chai and Y. G. Guo, *ACS Appl. Mater. Interfaces*, 2018, **10**, 22381-22388.
13. L. Xia, T. Long, W. Li, F. Zhong, M. Ding, Y. Long, Z. Xu, Y. Lei, Y. Guan, D. Yuan, Y. Zhang, C. Jia, L. Sun and Q. Sun, *Small*, 2020, **16**, e2003321.
14. H. R. Jiang, W. Shyy, L. Zeng, R. H. Zhang and T. S. Zhao, *J. Mater. Chem. A*, 2018, **6**, 13244-13253.
15. A. Mukhopadhyay, Y. Yang, Y. F. Li, Y. Chen, H. Y. Li, A. Natan, Y. Y. Liu, D. X. Cao and H. L. Zhu, *Adv. Funct. Mater.*, 2019, **29**, 1903192.
16. M. Jiao, T. Liu, C. Chen, M. Yue, G. Pastel, Y. Yao, H. Xie, W. Gan, A. Gong, X. Li and L. Hu, *Energy Storage Mater.*, 2020, **27**, 327-332.